Pergamon

Int. J. Heat Mass Transfer. Vol. 39, No. 5, pp. 1039–1049, 1996

0017–9310/96 $15.00+0.00

0017–9310(95)00183–2

Inverse finite element reduced mesh method for predicting multi-dimensional phase change boundaries and nonlinear solid phase heat transfer

R. G. KEANINI and N. N. DESAI

Department of Mechanical Engineering and Engineering Science, University of North Carolina
at Charlotte, Charlotte, NC 28223, U.S.A.

(*Received* 14 *December* 1994 *and in final form* 4 *May* 1995)

Abstract—An inverse finite element method is developed for simultaneous solution of multi-dimensional solid–liquid phase boundaries and associated three-dimensional solid phase temperature fields. The technique, applicable to quasisteady phase change problems, fixes element nodes at known temperature locations and uses a coarse, spatially limited mesh. This approach is designed to: (1) reduce direct and overall solution costs, (2) eliminate iterative direct solutions associated with temperature dependent thermophysical properties, (3) limit calculations to the heat affected zone and (4) eliminate *ad hoc* assumptions concerning the boundary heat flux distribution. The inverse algorithm couples a nonlinear solid phase conduction solver with conjugate gradient minimization. First-order regularization and upwind differencing are implemented to improve solution smoothness and stability and an analog welding experiment is used to investigate the technique's capabilities.

INTRODUCTION

Robust general purpose inverse solution procedures applicable to industrial scale phase change problems are nonexistent. Indeed, inverse phase change problems in general have received relatively limited attention [1–10]. This is somewhat surprising since the ability to predict multi-dimensional phase boundaries and associated solid temperature fields bears significantly on a number of important applications, including calculation of residual thermal stresses and strains [11], control of tissue destruction in high- and low-temperature surgical treatments [12], control of freezing and melting in cryopreservation protocols [13], and control of bead shape during welding [14]. Ultimately, such a capability may facilitate correlation of material microstructure with thermal history, may enhance process control, and may augment development of large-scale process simulations.

Progress has been hindered by three significant difficulties. First, since the number of grid points required for a given degree of spatial resolution can increase exponentially with spatial dimension, direct solution costs can also increase exponentially. Second, the number of parameters introduced in a realistic multi-dimensional inverse phase change problem typically increases with spatial dimension; geometric or even exponential increases in the number of parameters can easily occur. Importantly, overall solution costs increase with the number of unknown parameters. Third, while accurate inverse solutions often require incorporation of temperature dependent thermal properties, associated computational costs can be prohibitive.

The objective of this study is to develop an inverse method which allows relatively efficient inverse solutions to nonlinear multi-dimensional phase change problems. A new inverse method which simultaneously determines multi-dimensional phase change boundary shapes and associated solid phase temperature fields is formulated. In brief, the method defines a vector **P** which describes both the unknown phase boundary and the unknown boundary heat flux distribution. (As discussed below, the unknown boundary heat flux distribution, denoted by $P^{(q)}$ in Fig. 1, is determined at nodes labeled with interlocking Os and qs in Fig. 2. We will refer to the set $\mathbf{P}^{(q)}$ simply as the *boundary heat flux distribution*.) Beginning with an initial guess, $\mathbf{P}_o$, the inverse procedure iteratively alters **P** until the total error F between spatially discrete temperature measurements and corresponding calculated temperatures is minimized. Direct solutions are obtained using a nonlinear finite element conduction solver, while minimization is effected by the conjugate gradient method. Importantly, the direct solver uses a coarse, spatially limited mesh in which all nodal temperatures are experimentally known. This approach is designed to: (1) reduce direct solution costs; (2) eliminate iterative direct solutions associated with temperature dependent thermophysical properties; (3) limit calculations to the heat affected zone (HAZ) adjacent to the melt; and (4) eliminate *ad hoc* assumptions concerning the boundary heat flux distribution.

NOMENCLATURE

B	regularization term
c_p	specific heat
d_1, d_2, d_3; D_1, D_2, D_3	dimensionless and dimensional distances from the x-axis to the first, second and third columns of thermocouples
D_4	spacing (in the x-direction) between nodes not located on the melt boundary
e_{avg}	average relative error between calculated and experimental temperatures
e_{max}	maximum relative error between calculated and experimental temperatures
e_b	average absolute error between calculated and experimental boundary locations
h_u, h_m	dimensionless thermocouple embedding depths with respect to the plane $z = 0$
H	characteristic grid spacing
F	modified sum of squares error
k	thermal conductivity
L_z, L_z^o	solution domain thickness and workpiece thickness
M	number of parameters in $\mathbf{P}$ (Case I: $M = 10$; Case II: $M = 17$; Case III: $M = 31$)
N	number of temperatures used in inverse solution ($N = 48$)
N_b	number of parameters describing fusion boundary shape (Case II: $N_b = 7$; Case III: $N_b = 21$)
N_{bu}, N_{bm}, N_{bl}	number of parameters describing the fusion boundary shape on the planes $z = 0$, $z = h_m$ and $z = 2h_m$, respectively ($N_{bu} = N_{bm} = N_{bl} = 7$)
N_D	number of times that average temperatures from thermocouple array are obtained during an experiment ($N_D = 50$)
N_q	number of parameters describing boundary heat flux distribution on the planes $z = 0$ and $z = 2h_m$ ($N_q = 10$)
N_s	number of parameters describing fusion boundary on the back (or "straight") part of the pool (Case II: $N_s = 5$; Case III: $N_s = 15$)
N_{sp}	number of parameters describing the fusion boundary shape on any of the planes $z = 0$, $z = h_m$ and $z = 2h_m$ [equation (9)]
Pe_g, Pe_s	grid Peclet number ($Pe_g = u_pH/\alpha$) and solid Peclet number (u_pR_o/α)
$\mathbf{P}$	parameter vector
$P^{(bu)}, P^{(bm)}, P^{(bl)}$	parameters describing the fusion boundary shape on the planes $z = 0$, $z = h_m$ and $z = 2h_m$
$P^{(q)}$	parameters describing the boundary heat flux distribution on $z = 0$ and $z = 2h_m$
$q_o, \Delta q$	dimensionless constants used to define initial boundary heat flux
$r^{(u)}, r^{(m)}, r^{(l)}$	dimensionless initial parameter values for fusion boundary on the planes $z = 0$, $z = h_m$ and $z = 2h_m$, respectively
R_o	characteristic radius of heat source ($R_o = 2.0$ mm)
t_D	time interval between temperature measurements
Δt_D	sample time interval
$T, \hat{T}$	temperature and calculated temperature
T_m, T_∞	workpiece melting temperature and ambient temperature
u_p, U	dimensional and dimensionless workpiece travel speed ($U = 1$)
Y_i	measured temperature
x, y, z	dimensionless Cartesian coordinates, $x = X/R_o$, $y = Y/R_o$, $z = Z/R_o$
x'	dimensionless coordinate defined in Fig. 2
Δx_e	dimensionless node spacing in the x-direction
X, Y, Z	Cartesian coordinates.

Greek symbols

α	thermal diffusivity
Δr	dimensionless constant used to generate initial fusion boundary guess
ε	convergence tolerance
θ	dimensionless temperature, $\theta = (T - T_\infty)/(T_m - T_\infty)$
θ_e	experimental dimensionless temperature distribution on the non-melt vertical boundary
λ	regularization parameter
ρ	density
σ_i	standard deviation of ith temperature measurement.

Subscripts

avg	average
b	boundary
bl, bm, bu	lower, middle and upper boundary, respectively
D	data
e	experimental; vertical boundary
m	melting; middle
max	maximum
o	reference
u	upper
β	index.

Superscripts

bl, bm, bu	lower, middle and upper boundary, respectively
q	heat flux.

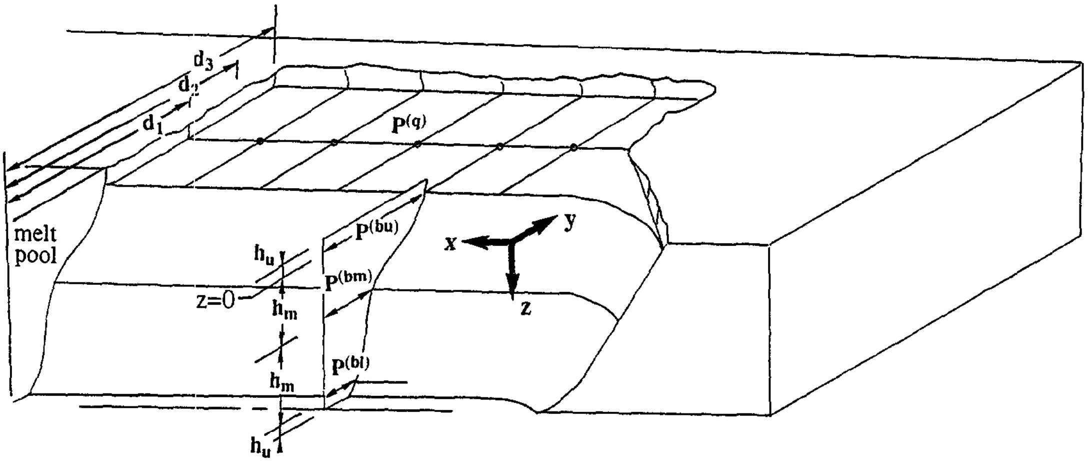

Fig. 1. Parameterization scheme and top view of finite element mesh. The heat source coincides with the z-axis and the x-axis coincides with the pool's centerline. Workpiece motion is in the positive x-direction. The solution domain's upper and lower boundaries lie at nondimensional depths h_u and h_u+2h_m below the workpiece's upper surface. The domain's middle layer lies at a depth h_u+h_m. Each of these depths are determined by thermocouple embedding depths within the workpiece. The nondimensional distances d_1, d_2 and d_3 are likewise determined by distances from the pool centerline to the embedded thermocouples. Parameterized heat fluxes ($P^{(q)}$) are defined at the five circled nodes on $z = 0$ and at five similar nodes on $z = 2h_m$.

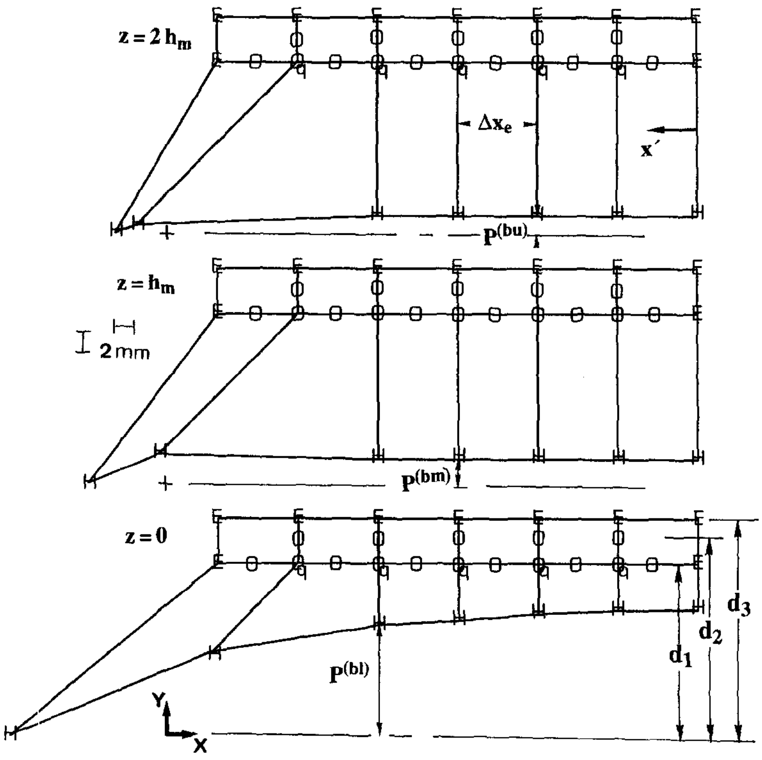

Fig. 2. Finite element mesh and locations of interpolated experimental temperatures (IETs) used in definition of F [equation (1)]. The N (= 48) IETs used in F are denoted by Os and interlocking Os and qs. Parameterized boundary heat fluxes are defined at the N_q (= 10) nodes labeled with interlocking Os and qs. IETs labeled by E are used as primary boundary conditions along the outer boundary. Similarly, temperatures at nodes on the melt boundary (labeled with H) are set equal to the workpiece melt temperature, T_m.

Due to these features, inverse solutions to realistic multi-dimensional phase change problems can be readily determined. Using a simple analog welding experiment, we examine inverse solutions under three sets of conditions:

Case I

Inverse solutions for the solid temperature field and boundary heat flux distribution are determined in the case where the three-dimensional melt boundary is known and fixed in the inverse code. (As discussed below and as shown in Fig. 2, the melt boundary on three planes within the workpiece is described by three sets of parameters, $\mathbf{P}^{(\mathrm{bl})}$, $\mathbf{P}^{(\mathrm{bm})}$ and $\mathbf{P}^{(\mathrm{bu})}$. Thus, in Case I, all three sets of shape parameters are fixed at their experimentally determined values.)

Case II

Inverse solutions for the interior fusion boundary shape ($\mathbf{P}^{(\mathrm{bm})}$ in Fig. 2), solid temperature field, and boundary heat flux distribution are determined when the melt shape is known and fixed on the upper and lower planes ($z = 0$ and $z = 2h_{\mathrm{m}}$ in Fig. 2). In circumstances where the upper and lower planes coincide (or nearly coincide) with outer, observable workpiece boundaries, this case corresponds to determining inner, nonvisible melt boundaries.

Case III

Preliminary results concerning inverse solutions for the complete three-dimensional (3D) fusion boundary and associated solid temperature field are discussed. The effect of the initial parameter specification on solution accuracy is examined in all three cases.

INVERSE ALGORITHM

The program uses conjugate gradient minimization to minimize the following modified sum of squares function [15]:

$$F(\mathbf{P}) = \sum_{i=1}^{N} (Y_i - \hat{T}_i(\mathbf{P}))^2 + \lambda B(\mathbf{P}) \qquad (1)$$

where $\mathbf{P} = (P_1, P_2, \ldots P_M)$ is the parameter vector, M is the number of parameters determined by the inverse solution, Y_i are N temperature measurements from various points within the solid region, $\hat{T}_i = \hat{T}_i(\mathbf{P})$ are corresponding calculated temperatures from the direct solution, λ is the regularization parameter, and $B(\mathbf{P})$ is the regularization term. $\mathbf{P}$ contains N_{b} parameters describing the unknown phase boundary and N_{q} ($= 10$) parameters describing the unknown boundary heat flux distribution. Thus, $M = N_{\mathrm{b}} + N_{\mathrm{q}}$. The parameterization scheme is shown in Fig. 1.

First order regularization is implemented using the following definitions of $\mathbf{B}$ in Cases II and III, respectively:

$$B = \sum_{i=1}^{N_{\mathrm{bm}}-1} (P_{i+1}^{(\mathrm{bm})} - P_i^{(\mathrm{bm})})^2 \qquad (2a)$$

$$B = \sum_{i=1}^{N_{\mathrm{bu}}-1} (P_{i+1}^{(\mathrm{bu})} - P_i^{(\mathrm{bu})})^2 + \sum_{i=1}^{N_{\mathrm{bm}}-1} (P_{i+1}^{(\mathrm{bm})} - P_i^{(\mathrm{bm})})^2 + \sum_{i=1}^{N_{\mathrm{bl}}-1} (P_{i+1}^{(\mathrm{bl})} - P_i^{(\mathrm{bl})})^2 \qquad (2b)$$

where $P_i^{(\mathrm{bu})}$, $P_i^{(\mathrm{bm})}$ and $P_i^{(\mathrm{bl})}$ are horizontal distances from the x-axis to the fusion boundary (refer to Fig. 1). The superscripts bu, bm and bl refer to the planes $Z = 0$, $Z = L_z/2$ and $Z = L_z$, respectively, while N_{bu}, N_{bm} and N_{bl} are the number of distances defined on each plane ($N_{\mathrm{bu}} = N_{\mathrm{bm}} = N_{\mathrm{bl}} = 7$).

The inverse program uses N spatially discrete measured temperatures as input and seeks to determine the unknown boundary shape and domain boundary heat flux distribution using the following algorithm:

(1) The conjugate gradient scheme alters the melt shape and boundary heat flux distribution.

(2) A finite element mesh is generated using the new fusion boundary.

(3) Using updated values of the boundary heat flux, a new temperature distribution is calculated on the updated mesh.

(4) The resulting direct solution allows calculation of a new value of F [based on equation (1)].

(5) If F is minimized, the program stops and a solution for the boundary shape, boundary heat flux distribution and the solid phase temperature field is determined. Otherwise, the program returns to step 1 and the process repeats.

In the following subsections, we outline the direct heat transfer problem, briefly discuss the finite element solution to the direct problem, and then describe numerical implementation.

Direct heat transfer problem

The direct heat transfer model is based on the following assumptions: (1) the workpiece moves past a stationary heat source at a constant speed u_{p}; (2) quasi-steady conditions prevail in the heat source-fixed coordinate system; (3) the problem is symmetric about the line of travel and (4) phase change occurs at a sharp, well defined temperature, T_{m}. (In cases where phase change occurs over a range of temperatures, the boundary temperature would be taken as the lowest temperature in the range.)

The problem domain is shown in Figs. 1 and 2. The heat source is centered on the Z-axis and the plate moves in the positive X-direction. Symmetry is assumed about the plane $Y = 0$. Defining the dimensionless temperature as

$$\theta = \frac{(T - T_\infty)}{(T_{\mathrm{m}} - T_\infty)} \qquad (3)$$

and scaling lengths by the characteristic heat source radius R_o ($= 2.0$ mm)

$$x = X/R_o \quad y = Y/R_o \quad z = Z/R_o \tag{4}$$

the non-dimensional conduction equation assumes the form:

$$U\theta_x = \frac{1}{Pe_s}\nabla\cdot[\tilde{k}\nabla\theta] \tag{5}$$

where $Pe_s = u_p R_0/\alpha$ is a generalized, temperature dependent solid Peclet number, T_∞ is the ambient temperature and $\alpha = k_0/(\rho c_p)$ is a generalized temperature dependent thermal diffusivity. Thermal conductivity, specific heat and density are temperature dependent; for convenience we express thermal conductivity as $k = k_o\tilde{k}$ where k_o is a constant and $\tilde{k} = \tilde{k}(\theta)$. The nondimensional velocity, U, equals one since the velocity scale is taken as u_p.

The temperature on the fusion boundary is the solid's melting temperature

$$\theta = 1 \tag{6}$$

while temperatures on the (non-melt) vertical boundaries equal experimentally measured temperatures:

$$\theta = \theta_e. \tag{7}$$

In addition, the upper and lower boundaries ($z = 0$ and $z = 2h_m$ in Figs. 1 and 2) are subject to the normal heat flux distribution defined by $\mathbf{P}^{(q)}$:

$$\frac{\partial\theta}{\partial z} = \kappa_0 P^{(q)} \tag{8}$$

where $\kappa_0 = R_o/(k(T_m - T_\infty))$.

Numerical methods

The problem described in equations (5)–(8) is solved using the Galerkin finite element method. Temperatures at every node are either specified (on the melt boundary) or interpolated from temperature measurements (see below). Iterative direct solutions are thus bypassed since temperature dependent thermophysical properties are known throughout the solution domain. In any given direct solution, primary boundary conditions along non-melt vertical boundaries (labeled with "E" in Fig. 2) are interpolated from experimental temperature measurements (described below). Primary boundary conditions are also imposed at nodes lying on the fusion boundary (labeled with "H" in Fig. 2). On the upper and lower surfaces, secondary (heat flux) boundary conditions, contained in vector $\mathbf{P}^{(q)}$, are imposed at nodes lying interior to the outer vertical edges and the fusion boundary (labeled with interlocking Os and qs in Fig. 2).

To ensure that all boundary shape parameters (i.e. distances) are either positive or zero and that the boundary does not intersect the thermocouple array, the following geometric constraints are imposed in Cases II and III:

$$P_\beta^{(bm)} \geqslant 0 \quad \beta = 1,\ldots,N_{sp} \quad \text{(Case II)} \tag{9a}$$

$$P_\beta^{(bu)} \geqslant 0 \quad P_\beta^{(bm)} \geqslant 0 \quad P_\beta^{(bl)} \geqslant 0$$
$$\beta = 1,\ldots,N_{sp} \quad \text{(Case III)} \tag{9b}$$

and

$$P_\beta^{(bu)} \leqslant d_1 \quad \beta = 1,\ldots,N_s \quad \text{(Case II)} \tag{10a}$$

$$P_\beta^{(bu)} \leqslant d_1 \quad P_\beta^{(bm)} \leqslant d_1 \quad P_\beta^{(bl)} \leqslant d_1$$
$$\beta = 1,\ldots,N_s \quad \text{(Case III)}. \tag{10b}$$

Here, d_1 is the dimensionless horizontal distance between the x-axis and the first column of thermocouples (parallel to the x-axis), N_s is the the number of parameterized distances describing the back ('straight') portion of the pool and N_{sp} ($= 7$) is the number of parameters describing the melt boundary on each of the planes $z = 0$, $z = h_m$ and $z = 2h_m$ (see Fig. 2). Constraints are imposed using nonexpansive projection operators on the convex sets defined by the constraints in equations (9) and (10) [16, 17].

The program requires an initial guess for $P_1, \ldots P_M$. Initial guesses for the fusion boundary shape on the planes $z = 0$, $z = h_m$ and $z = 2h_m$ are generated as follows:

$$P_\beta^{(bm)} = r^{(m)} + \Delta r\zeta \quad z = h_m \quad \text{(Case II)} \tag{11}$$

and

$$P_\beta^{(bu)} = r^{(u)} + \Delta r\zeta \quad z = 0 \tag{11a}$$

$$P_\beta^{(bm)} = r^{(m)} + \Delta r\zeta \quad z = h_m \tag{11b}$$

$$P_\beta^{(bl)} = r^{(l)} + \Delta r\zeta \quad z = 2h_m \quad \text{(Case III)} \tag{11c}$$

where $r^{(u)}$, $r^{(m)}$ and $r^{(l)}$ are constants and ζ is a random number between -1 and 1. The constant Δr can be adjusted to provide reasonably accurate ($\Delta r \ll 1$) or poor initial guesses ($\Delta r \sim O(1)$). In Case III it is found that inverse solution accuracy can be significantly enhanced by randomizing the initial shape specification through equations (11a)–(11c) (see also [17]). Other schemes for generating initial shape guesses were investigated; a heuristic condition on $\mathbf{P}_o$ is given in the Results and Discussion section below. The initial guess for the nodal surface heat flux is generated using

$$P_\beta^{(q)} = q_o + \Delta q\zeta \quad \beta = 1,\ldots,N_q \tag{11d}$$

where q_o and Δq are constants and again ζ is a random number between -1 and 1.

The regularization parameter, λ, is determined by finding the value that gives

$$\sum_{i=1}^{N}\left(\frac{Y_i - \hat{T}_i}{\sigma_i}\right)^2 \sim N$$

where σ_i is the standard deviation of the ith temperature measurement [15, 17]. Accordingly, λ is set equal to 0.01 in all cases. In all cases tested, essentially identical results are obtained using $\sim 5\times10^{-3} \leqslant \lambda \leqslant \sim 5\times10^{-2}$. In contrast, predicted fusion boundary shapes tend to become undulatory for $\lambda < \sim 5 \times 10^{-3}$, while non-physical solutions, reflecting dominance of the regularization term, result for $\lambda > \sim 5 \times 10^{-2}$.

The direct problem solution is obtained in the standard fashion. Element stiffness matrices and force vectors are calculated and assembled into their global counterparts. Primary boundary conditions are then introduced and the corresponding global equations condensed out. The condensed system is then solved using LU decomposition. Due to the coarseness of the mesh, the grid Peclet number, $Pe_g = Hu_p/\alpha_o$ (where H is the characteristic grid length and α_o is the thermal diffusivity at room temperature), is relatively large ($Pe_g \sim 5$). Thus, upwind differencing [18] is used to ensure stability. It should be noted that the scheme in [18] is subject to crosswind diffusion [19, 20] and that improved upwinding techniques are available [20–22]. However, as shown by Hughes and Brooks [19, 20], crosswind diffusion degrades accuracy only when elements are skew to the direction of travel, when boundary conditions are discontinuous, when workpiece motion is non-lineal, or when sources are present. Since workpiece motion is lineal, since boundary conditions are continuous, since there are no sources, and since elements in the problem are either not skew to the direction of travel or are only slightly skewed, Hughes' scheme [18] is expected to be accurate. This view is strongly supported by the accuracy of predicted temperature distributions and predicted phase boundary shapes (see below). Twenty-four linear brick elements containing 63 nodes are used in all calculations.

The inverse program stops when the following criterion is satisfied:

$$|F^{i+1} - F^i|/F^i \leqslant \varepsilon \tag{12}$$

where superscripts denote iteration number and where $\varepsilon = 10^{-8}$.

EXPERIMENTAL METHODS

An analog welding apparatus was constructed in order to validate the inverse procedure. Due to approximate dynamic similarity between paraffin and aluminum melts [23], and due to relative ease of handling, we chose paraffin as the workpiece material. As shown in Figs. 3 and 4, each paraffin block was fitted with nine thermocouples (Type K, 30 gage). Three rows ('rows' being parallel to the y-axis) of three thermocouples each were placed at three different depths within the workpiece. The first row, containing thermocouples 1–3, was embedded at a depth 2 mm below the workpiece's upper surface while the second and third rows (containing thermocouples 4–6 and 7–9) were placed 5 mm and 10 mm below this. The first, second and third thermocouples in each row were located at distances D_1, D_2, and D_3 ($= d_1 \cdot R_o, d_2 \cdot R_o, d_3 \cdot R_o$) from the X-axis (Fig. 3). The thermocouples were connected to an analog multiplexer and data acquisition was controlled by a PC-based data acquisition board (National Instruments, AT-MIO-16L-9); refer to Fig. 4. Due to the wax's low thermal diffusivity, workpiece motion was controlled by a PC-controlled fractional-step stepping motor, which provided speeds in the range 2×10^{-6} m s$^{-1} \leqslant u_p \leqslant 2 \times 10^{-2}$ m s^{-1}.

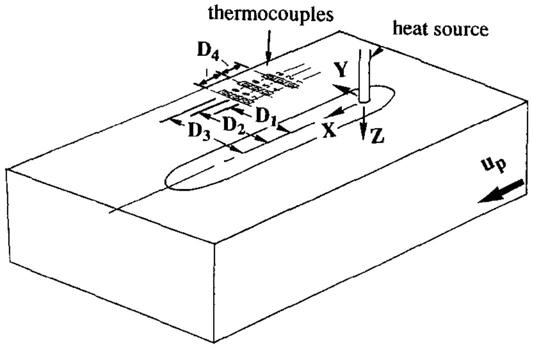

Fig. 3. Isometric view of thermocouple placement. $D_1 = 15$ mm, $D_2 = 17$ mm, $D_3 = 19$ mm and $D_4 = 2.3$ mm. Thermocouples 1–3, 4–6 and 7–9 are embedded at depths of 2, 7 and 12 mm, respectively. Workpiece thickness is 14 mm and $u_p = 1.24 \times 10^{-4}$ m s^{-1}.

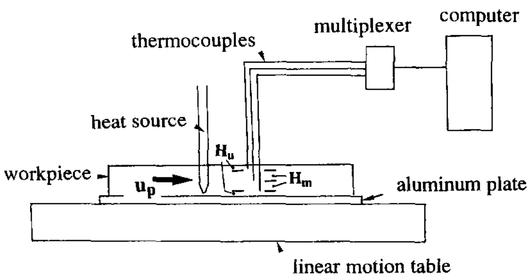

Fig. 4. Experimental set-up. Thermocouples 1–3, 4–6 and 7–9 are embedded at the respective depths $H_u = 2$ mm, $H_u + H_m = 7$ mm and $H_u + 2H_m = 12$ mm.

At the beginning of each experiment, the heat source was rapidly pushed to a fixed depth within the wax and plate motion initiated. The heat source, a soldering iron, was chosen to provide cross-sectional fusion boundary shapes resembling those in full penetration welds. During each experiment, average temperature readings from all nine thermocouples were obtained at N_D ($= 50$) equally spaced time intervals, t_D. Specifically, at each measurement time, $t_D, \ldots, N_D\, t_D$, the nine thermocouples were each sampled 70 times and the nine resulting averages saved on disk. This procedure was possible due to the data acquisition board's relatively high sample rate (10^5 Hz) and the plate's low travel speed ($u_p \sim 10^{-1}$ mm s^{-1}). Since the plate only moves on the order of 6 μm during any given sample interval, Δt_D ($\sim 5.6 \times 10^{-3}$ s), each set of stored average temperatures essentially reflects the instantaneous temperature distribution. Quasisteady conditions (in the heat source fixed coordinate system) were assumed when the melt assumed a constant width. Accordingly, only quasisteady temperatures were used in the inverse procedure.

Two sets of temperature measurements are required by the inverse code: the first set corresponds to the temperatures **Y** used to evaluate F in equation (1), while the second is used to impose the boundary condition in equation (7). Both sets are obtained by interpolating the stored temperatures described above. As shown in Fig. 2, finite element nodes are placed along the lines of travel traced out by the inner and outer columns of thermocouples in Fig. 3. Based on the sample rate (t_s^{-1}), the workpiece travel speed, and the initial array position, nodal temperatures on each of the planes $z = 0$, $z = h_m$ and $z = 2h_m$ are obtained by linearly interpolating between the nearest 'upstream' and 'downstream' temperature measurements. In the present case, the distance between adjacent (upstream and downstream) measurement locations (in the torch-fixed coordinate system) is 2.3 mm ($= D_4$) while node spacing in the x-direction (within the measurement volume) is 6 mm. The accuracy of this approach can be enhanced by either locating nodes at measurement locations or by increasing the sample rate. However, for purposes of illustration and due to the flexibility associated with adjustable node spacing (allowing inverse solutions over varying pool lengths), the present method is both adequate and attractive. The relative accuracy of predicted boundary shapes (discussed below) lends further support to this approach. Note that the uniqueness condition $N \geqslant M$ [24] is satisfied in all three test cases.

RESULTS AND DISCUSSION

Although placement of element nodes at known temperature locations effectively linearizes nonlinear direct problems, due to relatively small temperature changes and for purposes of illustration, constant thermophysical properties are used here. The following property values are assumed throughout [23]: $\rho = 814$ kg m^{-3}, $c_p = 2093$ J kg^{-1} K^{-1} and $k = 0.21$ J m^{-1} s^{-1} K^{-1}. Experimentally determined melting and ambient temperatures are $T_m = 31.0$°C and $T_\infty = 22.6$°C, while the workpiece travel speed is fixed at $u_p = 1.24 \times 10^{-4}$ m s^{-1}. The dimensional distances D_1, D_2, D_3 and D_4 and the thermocouple embedding depths are given in the caption to Fig. 3. The workpiece thickness, L_z^o, is 14 mm and (as mentioned) node spacing in the x-direction within the measurement volume is 6 mm. Experimental shapes on $z = 0$, $z = h_m$ and $z = 2h_m$ are directly measured by planing off wax to the desired depths at the conclusion of each experiment.

Case I. *Inverse solution when the melt shape is known and fixed in the inverse code*

In the first case, the fusion boundary is fixed to the experimentally determined shape and the parameter vector only includes the parameters describing the unknown boundary heat flux distribution. Thus, $M = 10$ and the regularization term B is set equal to 0. This case corresponds to the problem of determining solid phase temperature distributions and surface heat flux distributions given accurate information on the fusion boundary shape. Potential, though largely untested applications include post-process determination of 3D residual thermal stress and strain fields, correlation of HAZ microstructure or weld mechanical properties with thermal history, and post-process determination of surface heat flux distributions.

We examine solution accuracy as a function of the initial boundary heat flux specification by arbitrarily setting $q_o = 0$ in equation (11d) and obtaining solutions corresponding to $\Delta q = 0.1$, 1, 10, 10^2, 10^3 and 10^4. (Similar tests using $\Delta q = 0$ and $q_o = 0$, 1, 10, 10^2, 10^3 and 10^4 provide essentially identical final results.) Notice that the maximum initial (dimensional) parameter value is 10^4 times larger than the characteristic conductive heat flux $\kappa_o^{-1}(= k(T_m - T_\infty)/R_o)$, which is given following equation (8).

Experimental and predicted solid phase temperature fields corresponding to $\Delta q = 10^4$ are shown in Fig. 5. As shown, the difference between actual and predicted 3D solid temperature distributions is small. Similar results are obtained for $\Delta q = 0.1$, 1, 10, 10^2 and 10^3. Based on the work of Hughes and Brooks [19, 20], oscillations in the calculated temperature fields may be due to imposition of primary boundary conditions along the workpiece's trailing edge. In essence, the grid may be too coarse to resolve temperature variations (in the travel direction) near the trailing edge. Although the oscillations might be suppressed by imposing secondary (i.e. heat flux) boundary conditions along the trailing edge [19, 20], such a modification in the present study would introduce additional unknown heat fluxes into **P**. Thus, given the illustrative nature of this study and given that such modifications would, at best, provide only secondary

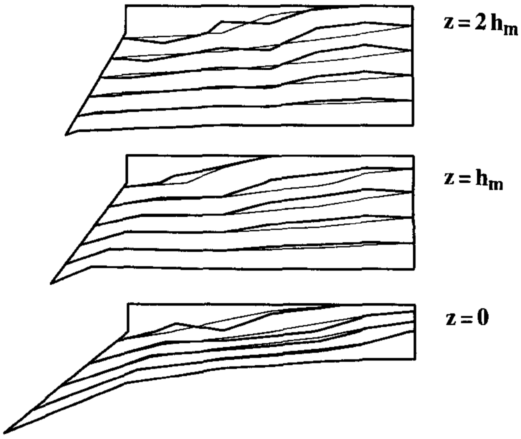

Fig. 5. Comparison between experimental (light lines) and calculated (heavy lines) temperature distributions, Case I. $\Delta q = 1 \times 10^4$ and $q_o = 0$. $e_{avg} = 2.4\%$, $e_{max} = 5.0\%$ and isotherm spacing is 1.9°C.

improvements in solution accuracy (given the accuracy of existing solutions), no modifications were attempted.

In order to assess the accuracy of any given solution, we define the maximum and average relative temperature errors as follows:

$$e_{\max} = \max\left(\frac{|Y_i - \hat{T}_i|}{Y_i}\right) \quad e_{\text{avg}} = \frac{1}{N}\sum_{i=1}^{N}\left(\frac{|Y_i - \hat{T}_i|}{Y_i}\right). \tag{13}$$

Based on these definitions, it is found that error in Case I remains virtually constant, with $e_{\max} \sim 4.9\%$ and $e_{\text{avg}} \sim 2.3\%$ for $0.1 \leqslant \Delta q \leqslant 10^4$. Thus, the inverse procedure is robust in this case, providing relatively low and essentially constant levels of error for every initial guess.

Predicted boundary heat flux distributions along the line segments $(Y, Z) = (D_2, 0)$; $X_1 \leqslant X \leqslant X_2$ and $(Y, Z) = (D_2, L_z)$; $X_1 \leqslant X \leqslant X_2$ are shown in Fig. 6 (here, X_1 and X_2 are the minimum and maximum X-coordinates of surface nodes having parameterized heat fluxes; refer to Fig. 2). Note that the left and right sides of the graph in Fig. 6 correspond respectively to the right- and left-most interior surface nodes in Fig. 2 (labeled with interlocking Os and qs). As indicated, nearly identical distributions are predicted for $\Delta q \leqslant 10$. For $\Delta q \geqslant 100$, predicted fluxes vary by up to 200% from those shown. We argue that the distribution shown is accurate since virtually identical distributions are obtained from widely varying initial guesses (i.e. $\Delta q = 0.1$, 1.0 and 10).

Case II. *Inverse solutions when the melt shape is known and fixed on the upper and lower planes,* $z = 0$ *and* $z = 2h_m$

In this case, the fusion boundary is fixed to the experimentally observed shape on the upper and lower planes, $z = 0$ and $z = 2h_{\text{m}}$. **P** thus describes the the melt shape on the center plane ($z = h_{\text{m}}$) and the normal heat flux distribution on $z = 0$ and $z = 2h_{\text{m}}$. Thus, $M = 17$ and the regularization term **B** [given by equation 2(a)] only includes the shape parameters on the middle plane. Since the ratio of embedding depth to workpiece thickness ($h_{\text{u}} \cdot R_{\text{o}}/L_z^{\text{o}}$) is either zero (surface temperature measurements) or much smaller than 1, melt shapes on $z = 0$ and $z = 2h_{\text{m}}$ can be directly observed or accurately estimated from the visible shape (assuming a full penetration melt). Thus, this problem has wider applicability than the first.

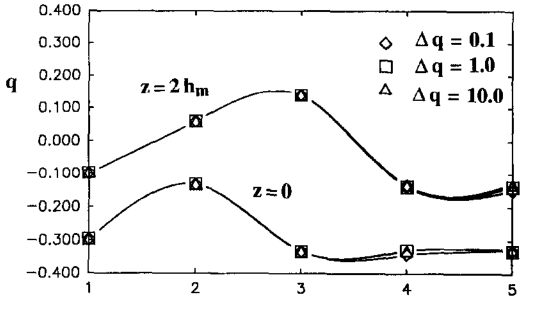

Fig. 6. Predicted dimensionless boundary heat flux distribution. The dimensionless coordinate x' and dimensionless node spacing Δx_{e} are defined at the top of Fig. 2. Thus, the right and left sides of this graph correspond to the left-most and right-most interior boundary nodes in Fig. 2 (which are labeled with interlocking Os and qs).

We examine solution accuracy as a function of the initial melt shape specification by arbitrarily setting $q_{\text{o}} = \Delta q = 0$ in equation (11d), $r^{(\text{m})} = 2.5$ in equation (11b), and by examining solutions corresponding to $\Delta r = 0$, 1.0, 2.0, 3.0, 4.0 and 5.0. To assess the accuracy of predicted shapes, we define the average difference between actual and predicted boundaries as follows:

$$e_{\text{b}} = \frac{1}{N_{\text{b}}}\sum_{1}^{N_{\text{b}}}\left(|r_i - \hat{P}_i^{(\text{b})}|\right) \tag{14}$$

where r_i is the ith measured boundary shape parameter, $\hat{P}_i^{(\text{b})}$ is the corresponding predicted value and N_{b} is the number of parameters describing the melt shape. (In this case, $N_{\text{b}} = 7$.)

Initial, predicted and experimental melt shapes and associated temperature fields for the case $\Delta r = 5.0$ are shown in Fig. 7. Similar results are obtained for the other Δrs tested. Similar to the results in Case I, average and maximum temperature differences, e_{avg} and $e_{\max}$, and average differences between predicted and experimental boundary parameters, e_{b}, are found to remain essentially constant over $0 \leqslant \Delta r \leqslant 5.0$, with $e_{\text{avg}} \sim 2.4\%$, $e_{\max} \sim 4.0\%$ and $e_{\text{b}} \sim 2.6\%$. Thus, the inverse procedure is again robust, providing essentially identical inverse temperature and shape solutions for every initial shape tested. Corresponding predicted nodal heat fluxes (not shown) differ by less than 3% from the nodal values shown in Fig. 6.

Case III. *Preliminary results concerning simultaneous inverse solutions for solid phase temperature fields and complete fusion boundary shapes*

Here, the parameter vector describes both the melt boundary and the boundary heat flux. Thus, $M = 31$ and B is given by equation (2b). Initial shape guesses are generated by assuming a linear depthwise variation in melt width superposed with a random component. Thus, $r_\beta^{(\text{u})} = 5.0$, $r_\beta^{(\text{m})} = 2.5$ and $r_\beta^{(\text{l})} = 0.0$ in equations (11a)–(11c) (where $\beta = 1, \ldots, 7$). Inverse solutions are then determined for Δr equal to 0.0, 1.0, 2.0, 3.0, 4.0 and 5.0. Note, in the current program, reasonably accurate solutions (satisfying $e_{\text{b}} \leqslant 0.1$) require that $r^{(\text{u})}$, $r^{(\text{m})}$ and $r^{(\text{l})}$ values lie within approximately 60–70% of actual values. The initial heat flux is specified as $q_{\text{o}} = \Delta q = 0$ in equation (11d).

Initial, predicted and experimental melt shapes and associated temperature fields for the case $\Delta r = 5.0$ are shown in Fig. 8. Similar results are obtained for the other Δrs tested. While inverse solutions are somewhat

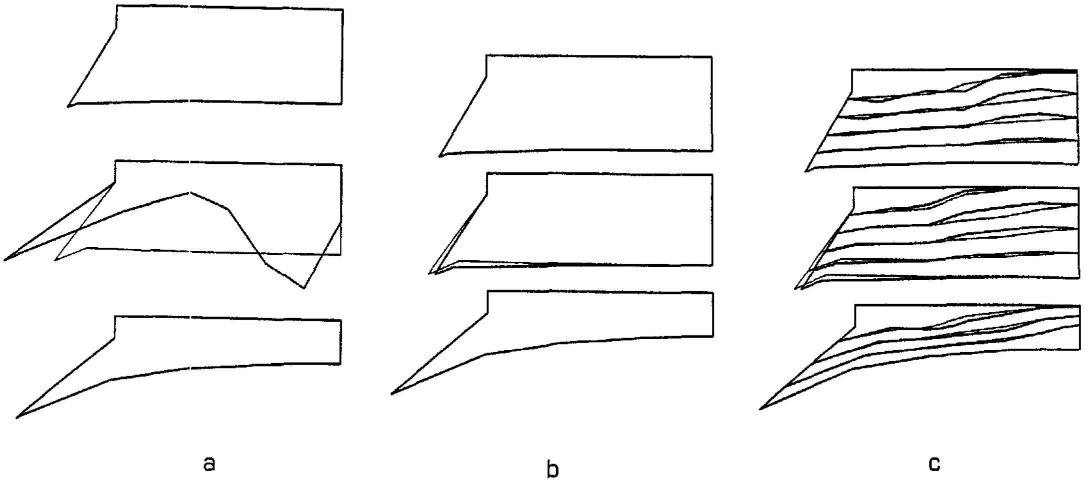

Fig. 7. Comparison between experimental (light lines) and predicted (heavy lines) interior melt shapes and solid phase temperature distributions, Case II. The guessed (heavy) and experimental (light) interior melt shapes on $z = h_m$ are shown in (a) while corresponding predicted (heavy) and experimental (light) shapes are shown in (b). Corresponding predicted and experimental temperature distributions are shown in (c). $\Delta r = 5$ and $q_o = \Delta q = 0$. $e_{avg} = 2.4\%$, $e_{max} = 4.0\%$ and $e_b = 2.6\%$. Isotherm spacing is 1.9°C.

accurate, the predicted boundary shape is too wide on the upper and center planes. Temperature distributions in the region between the melt boundary and the plane $y = d_1$ (d_1 is the distance from the x-axis to the first column of thermocouples in Fig. 2) correspondingly exhibit a fair degree of mismatch. In contrast, temperature fields within the measurement volume (between the planes $y = d_1$ and $y = d_2$) show good agreement. This last result is expected since F in equation (1) is based on temperature measurements from this volume. Associated errors, e_{avg}, e_{max} and e_b, fall within fairly narrow ranges: for $0 \leqslant \Delta r \leqslant 5.0$, $2.2\% \leqslant e_{avg} \leqslant 2.7\%$, $4.4\% \leqslant e_{max} \leqslant 6.9\%$ and $4.7\% \leqslant e_b \leqslant 7.5\%$.

Solution accuracy in the present experiment is essentially independent of the boundary heat flux. This feature is apparent since relatively accurate and nearly identical inverse solutions are obtained in every Case III test attempted; corresponding predicted heat fluxes, however, vary by up to 400% from those determined in Cases I and II (Fig. 6). This feature becomes particularly clear when considering Case I. There accurate temperature fields are obtained for all Δqs tested while predicted fluxes exhibit a 200% variation for $\Delta q \geqslant 100$. Physically, since the characteristic Biot number ($Bi = hR_o/k$) is only of the order of 10^{-2} to 10^{-1} (based on an estimated h of 1 to 10 W m^{-2} K^{-1} [25]), boundary information propagates by conduction to the measurement locations without significant interference (noise) from external heat fluxes.

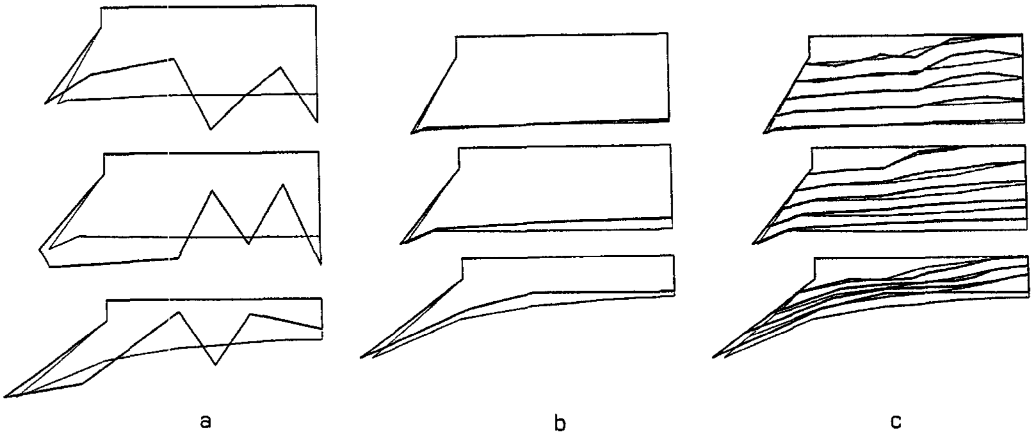

Fig. 8. Comparison between experimental (light lines) and predicted (heavy lines) melt shapes and solid phase temperature distributions, Case III. The guessed (heavy) and experimental (light) melt shapes are shown in (a) while corresponding predicted (heavy) and experimental (light) shapes are shown in (b). Corresponding predicted and experimental temperature distributions are shown in (c). $\Delta r = 5$ and $q_o = \Delta q = 0$. $e_{avg} = 2.2\%$, $e_{max} = 4.9\%$ and $e_b = 7.0\%$. Isotherm spacing is 1.9°C.

(Note, however, that measurement locations must be located within the thermal penetration zone surrounding the melt boundary, even when external boundaries are adiabatic and temperature measurements are noise free [10].) It is thus anticipated that inverse solution accuracy will be much more sensitive to the boundary flux in cases where one or more boundaries are subject to large heat inputs (e.g. welding) or losses (e.g. cryosurgery). In these cases, a hybrid inverse approach based on concurrent thermal and acoustic or electromagnetic sensing may be necessary.

Although the present set of results (Case III) are preliminary, the algorithm may provide sufficient accuracy for many applications, e.g. process control. Similarly, in cases demanding high accuracy, the algorithm could prove useful in generating accurate initial guesses for seeding larger inverse procedures (based, for example, on more temperature measurements on finer meshes).

CONCLUSIONS

An inverse method has been developed for predicting multi-dimensional phase change boundaries and associated 3D solid phase temperature distributions during quasi-steady phase change processes. The technique fixes finite element nodes at known temperature locations and relies on a coarse, spatially limited mesh. This approach is designed to effectively linearize nonlinear solid conduction problems and to reduce direct and overall solution costs. Upwind differencing is implemented to circumvent instabilities associated with large grid Peclet numbers while first-order regularization is used to enhance solution stability.

An analog welding apparatus is used to test the algorithm under three sets of conditions. In the first case, the parameterized melt shape is fixed at its experimentally observed location and solid phase temperature fields and boundary heat flux distributions are determined as a function of the initial heat flux specification. In the second case, the melt boundary is fixed at its experimentally observed location on upper and lower planes. The inner, nonvisible boundary, the solid phase temperature field, and the solid phase boundary heat flux distribution are then determined as functions of the initial interior melt shape specification. In the last, preliminary test case, inverse solutions for complete 3D melt shapes and solid temperature distributions are obtained as functions of the initial boundary specification.

Inverse solution accuracy is found to be insensitive to the boundary heat flux distribution. Due to the small ratio of convective to conductive heat transfer, boundary shape information propagates (subject to diffusive smearing) with little interference (noise) from external fluxes. This result suggests that multidimensional inverse phase change problems involving large external fluxes may be particularly difficult to solve. In these cases, hybrid inverse approaches based on concurrent thermal and acoustic or electromagnetic sensing may be necessary.

Acknowledgements—This work was supported by an Engineering Research Initiation Award (RI-A-93-06), sponsored by the Engineering Foundation and the American Society of Mechanical Engineers. The referees' comments and suggestions are particularly appreciated.

REFERENCES

1. M. A. Katz and B. Rubinsky, An inverse finite element technique to determine the change of phase interface location in one-dimensional melting problems, *Numer. Heat Transfer* **7**, 269–283 (1984).
2. M. Chun, H. Choi, H. Jun and Y. Kim, Phase-change front prediction by measuring the wall temperature on which solidification occurs, *Int. J. Heat Mass Transfer* **30**, 2641–2650 (1987).
3. C. S. Landram, Measurement of fusion boundary energy transport during arc welding, *J. Heat Transfer* **105**, 550–554 (1983).
4. Y. F. Hsu, B. Rubinsky and K. Mahin, An inverse finite element method for the analysis of stationary arc welding processes, *J. Heat Transfer* **108**, 734–741 (1986).
5. A. N. Alexandrou, R. Elden and J. McConnell, An inverse approach to three-dimensional solidification problems, *Int. J. Numer. Meth. Engng* **36**, 135–145 (1993).
6. Y. Ruan and N. Zabaras, Inverse finite element technique to determine the change of phase interface location in two-dimensional melting problems, *Commun. Appl. Numer. Meth.* **7**, 325–338 (1991).
7. D. J. McDaniel and N. Zabaras, Least-squares front-tracking finite element method analysis of phase change with natural convection, *Int. J. Numer. Meth. Engng* **37**, 2755–2777 (1994).
8. N. Zabaras, Y. Ruan and O. Richmond, Design of two-dimensional Stefan processes with desired freezing front motions, *Numer. Heat Transfer* **B21**, 307–325 (1992).
9. M. Samai, Y. Jarny and D. Delaunay, An optimization method using an adjoint equation to identify solidification front location, *Numer. Heat Transfer* **B23**, 67–90 (1993).
10. R. G. Keanini and B. Rubinsky, An inverse finite element minimization-based method for solution of multi-dimensional material and phase boundary shapes, *Int. J. Numer. Meth. Engng* **37**, 1125–1140 (1994).
11. J.-H. Kuang and A.-H. Liu, A study of the stress concentration factor on spot welds, *Welding J.* **69**, 468s–474s (1990).
12. R. G. Keanini and B. Rubinsky, Optimization of multiprobe cryosurgery, *J. Heat Transfer* **114**, 796–801 (1992).
13. B. Rubinsky and A. Shitzer, Analytical solutions to the heat equation involving a moving boundary with applications to the change of phase problem (the inverse Stefan problem), *J. Heat Transfer* **101**, 300–304 (1978).
14. B. Irving, EB welding joins the titanium fuselage of Boeing's F-22 fighter, *Welding J.* **73**, 31–36 (1994).
15. J. V. Beck, B. Blackwell and C. R. St Clair, Jr, *Inverse Heat Conduction—Ill-posed Problems*, pp. 134–145. Wiley, New York (1985).
16. J. Biemond, R. L. Lagendijk and R. M. Mersereau, *Proc. IEEE*, 856–883 (1990).
17. W. H. Press, B. P. Flannery, S. A. Teukolsky and W. T. Vetterling, *Numerical Recipes* (2nd edn), pp. 443–445, 795–806. Cambridge University Press, New York (1981).
18. T. J. R. Hughes, A simple scheme for developing 'upwind' finite elements, *Int. J. Numer. Meth. Engng* **12**, 1359–1365 (1978).
19. T. J. R. Hughes and A. Brooks, A multidimensional

upwind scheme with no crosswind diffusion. *Finite Element Methods in Convection Dominated Flows*, AMD-Vol. 34, pp. 19–36. American Society of Mechanical Engineers, New York (1979).

20. T. J. R. Hughes and A. Brooks, A theoretical framework for Petrov–Galerkin methods with discontinuous weighting functions: application to the streamline-upwind procedure. In *Finite Elements in Fluids*, (Edited by R. H. Gallagher, D. H. Norrie, J. T. Oden and O. C. Zienkiewicz), Vol. 4, Chap. 3. Wiley, New York (1982).
21. T. J. R. Hughes, Recent progress in the development and understanding of SUPG methods with special reference to the compressible euler and Navier–Stokes equations. In *Finite Elements in Fluids* (Edited by R. H. Gallagher, R. Glowinski, P. M. Gresho, J. T. Oden and O. C. Zienkiewicz), Vol. 7, Chap. 3. Wiley, New York (1988).
22. R. E. Bank, J. F. Burgler, W. Fichtner and R. K. Smith, Some upwinding techniques for finite element approximations of convection–diffusion equations, *Numerische Mathematik* **58,** 185–202 (1990).
23. Physics of variable-polarity plasma arc welding, NASA Tech Briefs, MFS-27207.
24. G. P. Flach and M. N. Ozisik, Inverse heat conduction problem of estimating spacially varying thermal conductivity and heat capacity per unit volume, *Numer. Heat Transfer* **16,** 249–266 (1989).
25. F. P. Incropera and D. P. Dewitt, *Fundamentals of Heat and Mass Transfer* (2nd edn), p. 433. Wiley, New York (1985).